Wave Breaking Dissipation Observed with 'SWIFT' Drifters

Jim Thomson *

* *Corresponding author address:* J. Thomson, Applied Physics Laboratory, University of Washington, 1013 NE 40th St, Seattle, WA 98105, USA.

E-mail: jthomson@apl.washington.edu

ABSTRACT

Energy dissipation rates during ocean wave breaking are estimated from high-resolution profiles of turbulent velocities collected within 1 m of the surface. The velocity profiles are obtained from a pulse-coherent acoustic Doppler sonar on a wave-following platform, termed a Surface Wave Instrument Float with Tracking, or 'SWIFT', and the dissipation rates are estimated from the structure function of the velocity profiles. The purpose of the SWIFT is to maintain a constant range to the time-varying surface and thereby observe the turbulence in breaking crests (i.e., above the mean still water level). The Lagrangian quality is also useful to pre-filter wave orbital motions and mean currents from the velocity measurements, which are limited in magnitude by phase-wrapping in the coherent Doppler processing. Field testing and examples from both offshore whitecaps and nearshore surf breaking are presented. Dissipation is elevated (up to 10^0 W/m^3 [$= 10^{-3}$ W/kg]) during strong breaking conditions, which are confirmed using surface videos recorded onboard the SWIFT. Although some velocity contamination is present from platform tilting and heaving, the structure of the velocity profiles is dominated by a turbulent cascade of eddies (i.e., the inertial sub-range). The noise, or uncertainty, in the dissipation estimates is shown to be normally distributed and uncorrelated with platform motion. Aggregated SWIFT measurements are shown to be useful in mapping wave breaking dissipation in space and time.

Contents

1. Introduction

The breaking of ocean surface waves generates strong turbulence and energy dissipation. In deep water, breaking participates in air-sea exchange and limits wave growth (Banner and Peregrine 1993; Melville 1996). In shallow water, breaking suspends sediment, forces currents, and drives coastal morphology (Battjes 1988). Although the mechanisms differ, both types of breaking are effective at dissipating wave energy in the form of turbulent kinetic energy (Herbers et al. 2000).

Field observations of deep water breaking (i.e., whitecaps) have shown that turbulent dissipation is a function of wave steepness and is correlated with wind stress (Terray et al. 1996; Gemmrich and Farmer 1999, 2004; Gerbi et al. 2009; Thomson et al. 2009; Gemmrich 2010). Field observations of shallow water breaking (i.e., surf) have shown that turbulent dissipation is a function of water-depth and is correlated with the energy flux gradient of shoreward swell (Trowbridge and Elgar 2001; Bryan et al. 2003; Feddersen 2011). These observations typically are made using fixed instruments mounted bellow the mean (still) water level. Thus, it has been difficult to estimate turbulent dissipation near the time-varying wave surface. Recently, Gemmrich (2010) used up-looking Doppler sonars to estimate dissipation within breaking wave crests and found dissipation rates ten times higher than those measured below the mean water level.

Here, the method of Gemmrich (2010) is adapted to wave-following reference frame using a new Lagrangian drifter. The drifter, which is termed a Surface Wave Instrument Float with Tracking (SWIFT), is designed to follow the time-varying free-surface while collecting high-resolution profiles of turbulent velocity fluctuations. The velocity fluctuations are used to estimate the turbulence dissipation rate following Wiles et al. (2006). Thus, the SWIFT measurements can be used to estimate both wave spectra (from the drifter motions) and wave breaking dissipation (from the Doppler velocity profiles). Previously, drifters have been used in the nearshore to observe currents (Schmidt et al. 2003; MacMahan et al. 2009), as well as particle dispersion (Spydell et al. 2007). Drifters also have been used in the open

ocean to observe wave breaking and air-sea exchange (Graber et al. 2000; Pascal et al. 2011). In addition to a Lagrangian reference frame, drifters have the advantage of measurement in the absence of ship interference (e.g., wave reflections from the hull).

The SWIFT platform and raw data collection are presented in §2. Then, processing methods for wave spectra and turbulent dissipation rates are described in §3, with an emphasis on separating platform motion from turbulence. These methods are demonstrated in §4 with data from two field tests: (a) shallow water surf at the Field Research Facility in Duck NC, and (b) deep water whitecaps on Lake Washington in Seattle WA. Examples from individual 'bursts' with strong and weak breaking are compared for each test, and results from all 'bursts' are aggregated to examine patterns in wave breaking dissipation. For the Lake Washington tests, an independent measurement of the wave-breaking turbulent dissipation rate at one point in the vertical profile is obtained using an acoustic Doppler velocimeter (ADV) onboard the SWIFT. Discussion of the test results and data quality follow in §5 and conclusions are given in §6.

2. Data collection

The Surface Wave Instrument Float with Tracking (SWIFT) is shown in Figure 1. The purpose of the SWIFT is to make measurements in a wave-following reference frame. The primary dimensions are: 2.15 m length overall (1.25 m draft + 0.9 m mast) and 0.3 m diameter hull. Onboard instruments include: a GPS logger (QStarz BT-Q1000eX), a pulse-coherent Doppler velocity profiler (Nortek Aquadopp HR), an autonomous meteorological station (Kestrel 4500), and a digital video recorder (GoPro Hero). The SWIFT location is tracked in realtime with a radio frequency transmitter (Garmin Astro). SWIFT missions typically last several hours, up to a full day, and data are collected in five-minute bursts.

a. Platform motion

The SWIFT wave-following motion is measured via GPS logger (QStarz BT-Q1000eX) at 5 Hz. Although the absolute horizontal accuracy of the DGPS positions is only 10 m, the relative horizontal velocity resolution is much higher (0.01 m/s) and suitable for the orbital motions of most ocean waves. The GPS vertical elevation accuracy is not sufficient to track wave-following motion, however relative (i.e., in the wave reference frame) vertical information is available from the pressure and orientation sensors in the Nortek Aquadopp HR. The Aquadopp pressure is equivalent to the SWIFT surface tracking, and pitch and roll are equivalent to the components of the SWIFT vertical tilting. (Constant values from these sensors indicate good wave-following behavior.) The GPS and Aquadopp orientation data are processed to determine the wave-height spectra and the quality of wave-following (see §3a).

In addition to wave-following motions, the SWIFT oscillates, or 'bobs', at a natural frequency. The SWIFT has 12.7 Kg buoyancy in the main hull (0.3 m diameter, see Figure 1) and 2.6 Kg of lead ballast at the bottom of the lower hull (i.e., 1.25 m below the surface). Following Middleton et al. (1976), the corresponding theoretical natural period is $T_n \approx 1.3$ s, which intentionally is shorter than most ocean waves. This natural oscillation is damped by a heave plate at the bottom of the lower hull (see Figure 1).

While wave-following, the SWIFT also drifts with mean currents and wind. Tests in Puget Sound, WA, under a range of tidal currents from 0.4 to 2.2 m/s, indicate drift velocities are consistent with fixed ADCP observations (not shown). Wind drag causes the SWIFTs to drift with the wind, which is measured onboard the SWIFT at 0.9 m above the surface, at about 5% of the wind speed (as empirically determined from tests in 0 to 14 m/s winds). While drifting, a sub-surface vane on the lower hull (see Figure 1) provides additional drag to maintain an orientation such that the video and Aquadopp beam 1 look upwind (or upwave, for locally generated wind-waves). Under strong winds, the drag of the 0.9 m mast causes a steady tilt of the SWIFT relative to the vertical (see picture in Figure 1). This tilt changes

slightly the vertical projection of sub-surface velocity profiles (next section), but otherwise has negligible effects.

b. Turbulence profiles, $u'(z)$

Turbulent velocity profiles $u'(z)$ are obtained with a 2 MHz Nortek Aquadopp HR (pulse-coherent) Doppler profiler. The Lagrangian quality of the drifter is motivated, in part, by range and magnitude limitations in the Doppler measurements of $u'(z)$. The Aquadopp is mounted in the lower hull and collects along-beam velocity profiles at 4 Hz with 0.04 m vertical resolution along a 0.8 m beam. Bursts of 1024 profiles (=256 s) are collected at 300 s intervals. The beam is orientated up and outward, at an angle of 25° relative to vertical (see Figure 1), and the SWIFT is vaned to keep this beam looking up-wave (to avoid measuring the drift wake of the SWIFT). In field testing, wave reflections from the main hull of SWIFT are not observed, presumably because the SWIFT is moving with the free surface. The blanking distance next to the transducer is 0.1 m, and thus the actual beam profile is 0.7 m long.

A major concern with up looking Doppler measurements is interference from surface reflections. This is especially significant for coherent systems. Profiles of alongbeam backscatter amplitude and coherence are used to look for interference, which would appear as a peak in amplitude and reduction in coherence at specific location in the profile (corresponding to a returning pulse interfering with an outgoing pulse). Using a pulse distance of 0.8 m, which is similar to actual distance to the surface, is the minimum value that can be used. Field testing (§4) does not indicate any interference for surface reflections.

The velocity data are quality-controlled using a minimum pulse correlation value of $c > 50$ (out of 100) and a minimum backscatter amplitude $a > 30$ counts, which were empirically determined to be the maximum values associated with spurious points and with bins out of the water. Nortek notes that a canonical value of $c > 70$ is often overly restrictive, and recommends $c > 50$ as a more useful cutoff (Rusello 2009). For Acoustic Doppler Velocimeter

(ADV) measurements, an accepted threshold is $c > 30 + 40\sqrt{f_s/f_{max}}$, where f_s and f_{max} are the actual and maximum possible sampling frequencies, respectively (Elgar et al. 2001; Feddersen 2010). Although ADVs are point measurements, instead of profile measurements, ADVs operate on the same coherent processing between pulse pairs to determine the Dopper shift and thus velocity. Applying the threshold here, using $f_s = 4$ Hz and $f_{max} = 8$ Hz, gives threshold of $c > 58$, similar to the ad hoc choice of $c > 50$. This choice of correlation cutoff is evaluated in §5 by comparing the sensitivity of results obtained in post-processing with cutoff values of $c > 0$, 25, 50, and 75.

Observations with $c < 50$ or $a < 30$ are assigned NaN velocity values and ignored during subsequent analysis (i.e., no interpolation). At worst, the quality control ratio of points removed to total points is 1:2, or half of the data in a given burst. Even in these cases with significant data removal, there are at least 512 profiles remaining with which to determine the average structure of the turbulence. More often, the quality control ratio is less than 1:10.

The velocity data also are quality-controlled by examining the Extended Velocity Range (EVR) data in the HR mode, which uses a second, shorter pulse lag to obtain a wider velocity range at point in the middle of the profile. Here, the pulse distances are 0.8 and 0.26 m, and the along-beam velocity range is 0.5 m/s. Comparing the profile and EVR data is essential to confirm that phase wrapping has not occurred. Comparing the profile and EVR data also is useful to evaluate quality-control via coherence and amplitude thresholds (i.e., for data within the velocity range, points with low correlations c or amplitudes a should be the only points that do not compare well).

The pulse-coherent measurements from the Aquadopp HR do not have a nominal Doppler uncertainty, or 'noise', value. Zedel et al. (1996) show that noise is a function of the coherence of each pulse pair, as well has sampling parameters (i.e., rate, number of bins) that control phase resolution. Still, a nominal value is useful when interpreting results. Here, a nominal velocity uncertainty (standard error) of $\sigma_{u'} = 0.025$ m/s is used, which is 5% of the along-

beam velocity range and similar to the $\sigma_{u'} = 0.02$ m/s reported by Zedel et al. (1996) for a correlation $c = 50$. In practice, the noise is not prescribed, but rather is retained as a free parameter in the solution for the dissipation rate (§3c). The empirical noise is later compared with the nominal variance of $\sigma^2_{u'}$ to evaluate results (§5).

The along-beam velocities are mapped, but not projected, to a vertical coordinate z for subsequent processing and plotting (i.e., each value of u' is unchanged, but is assigned a z location). The z location is defined as the distance beneath the instantaneous free surface ($z = 0$) and the Aquadopp pressure gage (also sampled a 4 Hz) is used to correct for any changes in the waterline level at the SWIFT. This correction is small (a result of the wave following nature of the platform), and never shifts the observed profile up or down more than one profile bin (i.e., ± 0.04 m).

3. Methods

The SWIFT drifters are designed to make in situ observations of velocity u that can be decomposed as

$$u = \bar{u} + \tilde{u} + u', \tag{1}$$

where $\bar{u}$ is the time mean velocity, $\tilde{u}$ are the wave orbital velocities, and u' are the turbulent fluctuations of velocity that are processed to estimate dissipation rates. In practice, the mean and wave orbital velocities are horizontal vectors in the earth reference frame, and the turbulence measurements are scalar along-beam components in the wave-following reference frame (see Figure 1). SWIFT data are parsed into five-minute bursts for processing, and $\langle\rangle$ notation will be used to denote burst ensembles. Overbars will be used for burst-averaged quantities. For example, the SWIFT GPS velocities are averaged to determine the mean drift velocity $\bar{u} = \langle u \rangle$. These bursts are sufficiently short to have quasi-stationary statistics (i.e., steady mean and variance), but long enough to have meaningful confidence intervals on calculated quantities. Given a typically drift speed of $\bar{u} \sim 0.2$ m/s, a SWIFT drifts

approximately 60 m during a burst. The burst-averaged quantities must assume homogeneity over this scale, which may be a poor assumption in a region of rapidly evolving waves (e.g., the surfzone).

The wave-following behavior of the SWIFTs, which separates wave orbital velocities $\tilde{u}$ from turbulent fluctuations u', is essential to the estimates of wave spectra and turbulent dissipation rates, respectively. These quantities, and the quality of wave-following, are described in the next two sections.

a. Frequency spectra, $S(f)$

Frequency spectra $S(f)$ are used to evaluate the motion of the SWIFT and to quantify the wave conditions. Spectra for each five-minute bursts are calculated as the ensemble average of the Fast Fourier Transform (FFT) of 16 sub-windows with 50% overlap, which resulting in 32 degrees of freedom and a frequency bandwidth $df = 0.0625$ Hz.

Spectra from Aquadopp orientation data (i.e., pitch, roll, and heading), $S_{\theta\theta}(f)$, are used to assess the tilting and turning of the SWIFT during wave-following. In field testing (§4), the orientation spectra $S_{\theta\theta}(f)$ does show broad peaks at the natural period of the platform and at the period of the waves. However, the more prominent signals are the trends caused by shifting winds and surface currents (i.e., low frequencies). These platform motions shift the entire Aquadopp profile $u'(z)$ with an offset Δu_θ, which has a negligible affect of the structure of $u'(z) - u'(z+r)$ (see next section).

Spectra from the Aquadopp pressure data (i.e., relative distance below the surface), $S_{pp}(f)$ are used to assess the surface tracking of the SWIFT during wave-following. In field testing (§4), the natural frequency (~ 0.7 Hz) is the dominant peak in the pressure spectra $S_{pp}(f)$, and wave peaks are negligible (i.e., pressure fluctuations from waves are absent in the wave-following reference frame). Integrating $S_{pp}(f)$ around the natural frequency estimates the variance in the surface tracking owing to 'bobbing' of the platform. In field testing, this variance is typically $O(10^{-4}$ m$^2)$, or a vertical standard deviation of 0.01 m.

In contrast, the SWIFT GPS horizontal velocity data contain the wave orbital motions relative to the earth reference frame. Thus, the wave orbital velocity spectra $\int S_{\tilde{u}\tilde{u}}(f)df = \langle (u - \bar{u})^2 \rangle$ is used to estimate the underlying wave conditions. The scalar wave height spectra $S_{\eta\eta}(f)$ can be calculated from $S_{\tilde{u}\tilde{u}}$ using linear finite-depth theory (Mei 1989), if the water depth is known from another source. In deep water, the conversion is simply $S_{\eta\eta}(f) = S_{\tilde{u}\tilde{u}}(f)(2\pi f)^{-2}$. In practice, this is done component-wise, with the total scalar spectrum equal to the sum of the converted spectrum of the two orthogonal velocity components.

Finally, spectra of the Doppler turbulent velocity profiles $S_{u'u'}(f)$ are used to look for contamination from SWIFT motion. Even for perfect wave-following, the $S_{u'u'}(f)$ spectra will have a peak at the natural frequency of the SWIFT, similar to the pressure spectra. For cases with significant tilt and rotation contamination, the $S_{u'u'}(f)$ spectra may have a peak at wave orbital frequencies as well. The relevant quantity for estimating turbulent dissipation, however, is the difference between points in the velocity profile $u'(z) - u'(z + r)$ (see next section). The velocity differences (i.e., the turbulence) along a profile are much less susceptible to motion contamination, because platform motion contaminates the entire profile (i.e., an offset). Thus, spectra of velocity differences at selected points along the profile are used to evaluate the motion contamination of the turbulence observations. In field testing (§4), velocity spectra show expected peaks, however velocity difference spectra lack wave or natural frequency peaks. The velocity difference spectra depend on the separation distance between velocity bins, and an increase in spectral energy density with increasing separation is consistent with the structure of a turbulent cascade.

b. Turbulence structure function, $D(z, r)$

The along-beam Doppler velocity profiles $u'(z)$ are processed to estimate the turbulent dissipation rate following the method of Wiles et al. (2006), in which the vertical second-order

structure function $D(z,r)$ of velocity fluctuations $u'(z)$ is defined as

$$D(z,r) = \left\langle (u'(z) - u'(z+r))^2 \right\rangle, \tag{2}$$

where z is the vertical location beneath the free surface, r is the along-beam distance between velocity fluctuations, and the bracket denotes the burst time-average (five minutes). This choice of time-scale obscures the details of a individual breaking events in favor of robust statistics on the overall effect of breaking (enhanced turbulent dissipation near the free surface). Note that variance in time is not significant to the structure function, other than as contamination by non-stationarity, because it is the difference of $u'(z)$ over spatial scales r that controls $D(z,r)$.

$D(z,r)$ is one-sided, such that differences are taken from the top of the profile downwards, and at least three valid velocity bins (i.e., three $z+r$ combinations) are required to obtain each $D(z,r)$ value. The range r is limited to half of the profile length or the distance to the boundary, whichever is smaller. As shown by Gemmrich (2010), estimation of the structure function beneath breaking waves is sensitive to the maximum separation scale $|r|$ used, because turbulence may decay rapidly beneath the wave crests (i.e., heterogeneity).

c. Dissipation rate profiles, $\bar{\epsilon}(z)$

Assuming homogenous turbulence and a cascade of isotropic eddies in the inertial subrange (Kolmogorov 1941), the dissipation rate of turbulent kinetic energy scales as $\epsilon \sim u'^2/T \sim u'^3/r$, where T is a time scale given by r/u'. Thus, the structure of the turbulence $D(z,r)$ should follow a power law $r^{2/3}$. Here, the burst estimates of $D(z,r)$ are fit to a linear model

$$D(z,r) = A(z)r^{2/3} + N, \tag{3}$$

where an A is determined for each z using MATLAB's robust fit algorithm and N is an offset due to measurement noise. The burst-averaged dissipation rate is then

$$\bar{\epsilon}(z) = \rho_w \mathcal{C}_v^{-3} A(z)^{3/2}, \tag{4}$$

where $\mathcal{C}_v$ is a constant equal to 1.45. The offset N is expected to be $2\sigma_{u'}^2$, in which $\sigma_{u'}$ is the Doppler noise of the velocity measurement (Wiles et al. 2006; Rusello and Cowen 2011). Here, N values are obtained from robust linear fit (rather than prescribed) and are used to evaluate errors in the methods or violations in the assumptions (see §5). The N values are also used for quality control, by accepting only $N \ll Ar^{2/3}$.

The room-mean square error (RMSE) between the fitted $A(z)r^{2/3}$ and the actual structure $D(z,r)$ is propagated through Eq. 4 and used as the uncertainty in dissipation σ_ϵ. This uncertainty is asymmetric, because of the exponent in Eq. 4, and both upper and lower bounds are propagated as $\sigma_{\epsilon\pm}$. This uncertainty is used for another layer of quality control, by requiring that $|\sigma_{\epsilon\pm}| \ll \epsilon$.

The dissipation rate profile $\bar{\epsilon}(z)$ can be integrated to obtain the total dissipation rate per unit surface area,

$$\bar{E} = \int \bar{\epsilon}(z) dz. \tag{5}$$

This integral is limited by the lowest depth ($z \approx 0.5$ m) below the wave-following surface ($z = 0$ m). For some wave conditions, this limitation will be severe given the expectation that the depth breaking turbulence scales with wave height (Babanin 2011). However, in field testing (next section), dissipation rates are observed to decrease sharply beneath the wave following surface and linear extrapolation below $z = 0.5$ would rarely increase $\bar{E}$ more than 10%. This is consistent with Gemmrich (2010), in which near-surface profiles of wave-resolved dissipation rates captured the full evolution of breaking turbulence within $z < 0.6$ m. The uncertainties $\sigma_{\epsilon\pm}$ are summed in Eq. 5 to obtain asymmetric uncertainties in the 'total' dissipation, $\sigma_{E\pm}$.

Finally, in some of the field testing, another method to estimate the dissipation rate is incorporated to provide an independent comparison with the structure function method. The second method uses the common approach of rapidly sampled (32 Hz) acoustic Doppler velocimeter (ADV) data to calculate frequency spectra of turbulent kinetic energy (Lumley and Terray 1983; Trowbridge and Elgar 2001; Feddersen 2010). The frequency spectra are

converted to wavenumber spectra by assuming the advection of a frozen field (i.e., Taylor's hypothesis), and the dissipation rate is obtained by fitting an amplitude B to the inertial sub-range of the spectra, $S_{ADV}(f) = Bf^{-5/3}$, and taking $\bar{\epsilon}_{ADV} = \rho_w \left(\frac{B}{(\bar{u}/2\pi)^{2/3}\kappa}\right)^{3/2}$. For implementation on the SWIFT, a Nortek Vector ADV was mounted at $z = 0.25$ m below the surface (see Figure 1), and the GPS-based drift velocity was used for the advection velocity $\bar{u}$. The Kolmogorov constant is $\kappa = 0.55$, and the RMSE in the fit is propagated to obtain asymmetric uncertainties on the $\bar{\epsilon}_{ADV}$ values (similar to the approach for uncertainties in $\bar{\epsilon}$ from the structure function). The ADV method only estimates dissipation a single depth beneath the surface ($z = 0.25$ m), and thus is insufficient to evaluate the total dissipation (Eq. 5).

4. Field testing and examples

A series of field tests have been conducted to refine the SWIFT design and data processing algorithms. To date, six SWIFTs have been fabricated and approximately 400 hours of SWIFT data have been collected in testing. Select data and results from tests are presented in the following sections. First, shallow-water testing at the Duck Field Research Facility (FRF) is described. Second, deep-water testing on Lake Washington is described, which includes the ADV spectral dissipation estimates (for comparison with the Aquadopp HR estimates via the structure function). For each field test, individual burst data and processing are compared between weak and strong breaking conditions (as determined from the onboard video recordings), and then patterns from aggregate results using all bursts are examined.

a. Shallow-water breaking (surf) at Duck FRF

Field data were collected over four hours on 15 September 2010 at the US Army Corps of Engineers (US-ACE) Field Research Facility (FRF) in Duck, NC (USA). Conditions, as measured by FRF instruments were: onshore 2-5 m/s winds, 10 s period swell with 0.6 m

significant wave height. The FRF uses a local coordinate system, in which x is increasing offshore and y is increasing alongshore. For these mild conditions and neap tides, the surfzone was contained with $100 < x < 150$ m. SWIFTs were released from a small boat outside of the surf zone (cross-shore distance $x \sim 250$ m, water depth $h \sim 4$ m) and allowed to drift into the surf zone. SWIFTs eventually grounded on the beach and were recovered there. An early version of the SWIFT was used, which differed slightly from the version in Figure 1. The earlier version used a 90° transducer head on the Aquadopp HR, which was mounted across the lower hull to achieve approximately the same beam geometry as the version in Figure 1. All other sampling parameters were as described in previous sections.

Figure 2 show examples of the raw burst data (4 Hz for 5 minutes) from outside and inside of the surf zone (left versus right panels). The surface elevation ($z = 0$) appears constant in the lower panels because the SWIFT is following the free-surface. There is a notable decrease in scatter for velocity measurements above the chosen correlation cutoff $c > 50$ (upper panels of Figure 2). There also is improved agreement between the profile data and the extended velocity range (EVR) data for velocity measurements above the chosen correlation cutoff $c > 50$ (middle panels of Figure 2). The depth profiles of do not show any strong trends (lower panels of Figure 2). In particular, the profiles of amplitude and correlation did not show any sharp features that would indicate interference from surface reflections. The backscatter amplitude is uniformly increased in the surf zone example ($a \sim 200$ counts) compared with the offshore example ($a \sim 150$ counts), consistent with the presence of bubbles in the surf zone. The burst data outside of the surf zone include a brief period (~ 20 s) with the instrument out of the water for repositioning, and this results in a much higher quality control ratio (i.e., more points are removed from the velocity data prior to processing).

Figure 3 shows examples of the spectra estimated from outside and inside of the surf zone (left versus right panels). For this test, SWIFT GPS data were not sufficient quality to estimate wave spectra, and wave spectra from a nearby FRF array instrument (an Aquadopp

at $x = 232$ m) are used. The SWIFT orientation spectra show a trend of more variance at lower frequencies, with no distinct peaks (upper panels of Figure 3). The SWIFT pressure spectra show an expected peak at a natural frequency of $f_n \approx 0.7$ Hz and no peak at wave frequencies, consistent with surface following motion (middle panels of Figure 3). The turbulent velocity spectra of a selected depth $z = 0.16$ m below the surface do show a peak at the natural frequency of the SWIFT, indicating the potential for motion contamination. However, the two selected velocity differences (between depths $[z, z + 0.04\text{m}]$ and $[z, z + 0.16\text{m}]$) do not show contamination peaks (lower panels of Figure 3). Moreover, the velocity difference spectra show an expected increase in energy density between smaller $(z, z+0.04\text{m})$ and larger $(z, z + 0.16\text{m})$ lag distances. It is these velocity differences that determine the structure function $D(z, r)$ and associated dissipation rates (Eqs. 2-4).

Figure 4 shows examples of the processing of turbulent velocity profiles outside and inside of the surf zone (left versus right panels). The structure function $D(z, r)$ is fit to $Ar^{2/3}$ at different depths z, and the slope A increases inside the surf zone (left versus right middle panels of Figure 4). The noise intercept N is small for all fits, and the RMSE error between the fits and the structure function is small. The resulting dissipation rate profiles $\bar{\epsilon}(z)$ are well-resolved and decrease away from the surface (lower panels of Figure 4). The depth-integrated dissipation rate $\bar{E}$ in the surfzone is approximately 2.5 times larger than outside of the surfzone.

Figure 5 shows cross-shore bathymetry and the aggregated results of all SWIFT bursts on 15 September 2011, plotted as a function of cross-shore distance in the local FRF coordination system. With small incident waves and a weak (neap) low tide, the surfzone is at approximately $100 < x < 150$ m. (With larger waves and lower tides, the surfzone typically is farther offshore.) The vertically integrated dissipation rate estimates $\bar{E}$ peak within the surfzone (middle panel of Figure 5). These 'total' dissipation rates likely neglect important significant dissipation occurring near the seabed (Feddersen 2011), which is discussed further in §5. In contrast, the noise in the structure function fits does not increase in the surf

zone (lower panel of Figure 5), suggesting that noise is not correlated with the dissipation estimates, nor the SWIFT motions (both of which increase in the surf zone).

b. Deep-water breaking (whitecaps) on Lake Washington

Field data were collected over six hours on 12 November 2011 on Lake Washington in Seattle, WA (USA). Conditions, as measured by nearby meteorological station (King County bouy) and Waverider instruments were: southerly 8-10 m/s winds, 3 s period fetch-limited waves with 0-1 m significant wave height. SWIFTs were released from a small boat just north of the I-90 floating bridge in the middle of the lake and allowed to drift north along a fetch distance x, where $x = 0$ is the location of the floating bridge. SWIFTs were in deep water ($h > 30$) m at all times, as confirmed via post-processing of GPS positions with bathymetry in Google Earth. As shown in Figure 1, this version of SWIFT included an Acoustic Doppler Velocimeter (ADV) sampling at a single bin in the middle of the Aquadopp HR profile.

Figure 6 shows example burst data with mild breaking at short fetch and strong breaking at long fetch (left versus right panels). The surface elevation ($z = 0$) appears constant in the lower panels because the SWIFT is following the free-surface. The scatter for velocity measurements is similar above and below the chosen correlation cutoff $c > 50$, as is the agreement between the profile data and the extended velocity range (EVR) data (upper panels of Figure 6). The depth profiles of do not show any strong trends (lower panels of Figure 6). In particular, the profiles of amplitude and correlation do not show any sharp features that would indicate interference from surface reflections. The amplitude increases slightly near the surface, possibly consistent with bubble injection by wave breaking (whitecaps).

Figure 7 shows examples of the spectra estimated during mild breaking and during strong breaking (left versus right panels). The SWIFT orientation spectra show a trend of more variance at lower frequencies, with broad response coinciding with the peak waves (upper panels of Figure 7). The wave spectra from the SWIFT GPS show wind-waves at $f = 0.3$ Hz (middle panels of Figure 7), consistent with nearby Waverider measurements. The SWIFT

pressure spectra show an expected peak at a natural frequency of $f_n \approx 0.7$ Hz and no peak at wave frequencies, consistent with surface following motion (middle panels of Figure 7). The turbulent velocity spectra of a selected depth $z = 0.16$ m below the surface do show a peak at the natural frequency of the SWIFT, indicating the potential for motion contamination. However, two selected velocity differences (between depths $[z, z + 0.04\text{m}]$ and $[z, z + 0.16\text{m}]$) do not show contamination peaks (lower panels of Figure 7). Moreover, the velocity difference spectra show an expected increase in energy density between smaller $(z, z + 0.04\text{m})$ and larger $(z, z + 0.16\text{m})$ lag distances. It is these velocity differences that determine the structure function $D(z, r)$ and associated dissipation rates (Eqs. 2-4).

Figure 8 shows examples of the processing of turbulent velocity profiles during mild and strong breaking (left versus right panels). The structure function $D(z, r)$ is fit to $Ar^{2/3}$ at different depths z, and the slope A increases during stronger breaking (middle panels of Figure 8). The noise intercept N is small for all fits, and the RMSE error between the fits and the structure function is small. The resulting dissipation rate profiles $\bar{\epsilon}(z)$ are well-resolved and decrease away from the surface (lower panels of Figure 8). The estimates from the ADV at $z = 0.25$ m are consistent with structure function estimates at the same depth below the wave-following surface (although it must be noted that the largest values of $\bar{\epsilon}(z)$ are all closer to the surface and thus not evaluated by the ADV comparison). The depth-integrated dissipation rate $\bar{E}$ during strong breaking (farther along the fetch) is approximately 2.5 times larger than during mild breaking (at short fetch).

Figure 9 shows the aggregated results of all SWIFT bursts on 12 November 2011, plotted as a function of north-south fetch distance x along Lake Washington. Wave heights, as estimated from the SWIFT GPS spectra, increase along the fetch from 0.2 m to 0.9 (upper panel of Figure 9). The vertically integrated dissipation rate estimates $\bar{E}$ increase along the fetch from 0.1 W/m^2 to 1.0 W/m^2 (upper-middle panel of 9). In contrast, the noise in the structure function fits does not increase along the fetch (lower-middle panel of Figure 9), which suggests the noise is not correlated with the dissipation estimates, nor with the

SWIFT motions (both of which increase with fetch). The ADV estimates of dissipation at $z = 0.25$ m are consistent with the profile estimates $\bar{\epsilon}(z)$ along most of the fetch (lower panel of Figure 9).

5. Discussion

In this section the magnitude and depth dependence of the dissipation rates during field testing are compared with literature values and simple models. Then, errors and uncertainties in the dissipation rates are discussed, as well as sensitivity to the correlation cutoff applied to the Doppler velocity measurements.

a. Scaling of dissipation rates

The dissipation rate profiles observed at both the Duck FRF (surf breaking) and on Lake WA (whitecap breaking) decrease with depth beneath the free surface (i.e., lower panels of Figures 4 & 8). In the absence of wave breaking (i.e., offshore of the surf zone at the Duck FRF or at very short fetch on Lake WA), the linear decrease is qualitatively consistent with the well-known wall-layer dependence $\bar{\epsilon}(z) = u_*^3/(\kappa_v z)$, where u_* is the friction velocity and κ_v is the von Karman constant, as shown by (Agrawal et al. 1992). During breaking, the decrease in dissipation rate with depth is consistent with conceptual models for a source of turbulence that diffuses beneath the surface (e.g., Craig and Banner (1994)). At the Duck FRF, the depth dependence is weak, suggesting that diffusion is strong. On Lake WA, the depth dependence is stronger and suggests that wave-breaking turbulence is isolated to within 0.2 m of the surface, consistent with previous observations that whitecap turbulence is largely contained to a depth less than the wave height (Terray et al. 1996; Gemmrich 2010). This depth scaling will be evaluated further in a future paper, including comparisons with models for the direct injection of wave-breaking turbulence (as opposed to diffusion).

The 'total' dissipation rates observed at the Duck FRF can be compared to a simple

energy budget for the incoming swell. Requiring the energy flux per crest length, $F = \rho_w g\sqrt{gh}\int S_{\eta\eta}(f)df$, to be dissipated through a surf zone of cross-shore width x_{sz}, the average dissipation rate per unit surface area is F/x_{sz} (Mei 1989). Using the wave conditions observed at the FRF Aquadopp in $h = 3$ m water depth and $x_{sz} \approx 50$, the expected average dissipation is 50 W/m^2. This value far exceeds the average 'total' dissipation obtained from the SWIFT within the surf zone ($\bar{E} \sim 0.2$ W/m^2). Previous studies also have estimated surf zone dissipation rates much less than the expected energy flux gradient (Trowbridge and Elgar 2001; Bryan et al. 2003; Feddersen 2011). Here, some of the difference may be explained by dissipation occurring below $z = 0.5$ m, especially near the seabed where Feddersen (2011) finds local dissipation rates in a saturated surf zone as high as 3 W/m^3 (i.e., similar order of magnitude to the near-surface SWIFT values in the Duck FRF surf zone). In addition, during this neap tide and mild waves, many waves did not break until reaching the steep foreshore ($x < 100$ m in Figure **??**), where they are not captured by SWIFT measurements and where wave reflection may account for up to 30% of the incident swell energy flux (Elgar et al. 1994). Finally, energy flux also may be lost to mean currents (longshore and cross-shore) in the surf zone.

Another significant bias of the SWIFT surf-zone values may be the five-minute burst averaging, since the dissipation rates in the surf zone are event driven and unlikely to be normally distributed. Alternate averaging (e.g., log-normal) in Eq. 2 produces similar results for these field tests, suggesting the intermittence cannot be simply treated. The breakpoint of an irregular wave field on a natural beach is not well-defined; some waves may break further shoreward and some may break further seaward. Thus, even for a five-minute burst when the SWIFT is drifting within 10 m (cross-shore distance) of the nominal breakpoint, breaking (and presumably maximum dissipation) may only be observed for a few waves. This demonstrates the need for fixed instruments (Eulerian measurements) to interpret the SWIFT estimates. The surf-zone energy balance will be evaluated further in a future paper.

The 'total' dissipation rates observed on Lake WA can be compared to a simple energy

budget for wind forcing. Under equilibrium conditions (i.e., steady state fetch-limited wave field), the wind input rate W equals the 'total' dissipation rate $\bar{E}$. Since whitecapping is more regular, with uniform breaking rates of 1-2 per minute in a strongly forced sea state, the five-minute burst average $\bar{E}$ from SWIFT methods is better suited to this cases (compared with intermittence in the surf-zone). Locally generated wind waves are forced by a wind stress $\tau = \rho_a C_D U_{10}^2$, where ρ_a is the density of air, U_{10} is the wind speed at a reference height of 10 m, and C_D is a drag coefficient that depends on wave age and wind speed (Donelan et al. 1993). The rate of energy input to the waves is estimated as a continuous stress acting on a surface moving at an effective speed c_e, such that (Gemmrich et al. 1994; Terray et al. 1996) $W = c_e\tau = c_e\rho_a C_D U_{10}^2$, where W is that rate of energy input per area of the sea surface, and the phase speed of the peak waves c_p is used for c_e. For the Lake WA tests, the wind input is approximately $W \sim 2$ W/m^2, which is similar to the $\bar{E} \sim 1$ W/m^2 obtained from the SWIFT measurements. These energy balances will be evaluated further in a future paper, including alternatives to the $W = c_e\tau = c_p\tau$ assumption.

Finally, it must be noted that there are many sources of turbulent dissipation at the air-sea interface. The SWIFT-based estimates are the 'total' dissipation rate in the upper 0.5 m of the ocean, and the above energy budgets attribute all of this dissipation to breaking waves. To successfully isolate the breaking contribution, it may be necessary to remove a non-breaking offset, which is estimated a priori, measured independently, or assumed to be the lowest value in the profile.

b. Errors and uncertainty in dissipation rates

There are three inter-related potential sources of error in the dissipation estimates: 1) errors introduced by SWIFT motion, 2) errors in the fit to the spatial structure of an assumed turbulence cascade, and 3) errors in the pulse-coherent Doppler velocity measurements.

Motion contamination is quantified using frequency spectra. There are no observed spectral peaks in the difference between velocity bins, although there are SWIFT motion

peaks for individual velocity bins (see Figures 3 & 7). Thus, the structure function (Eq. 2) is unlikely to be contaminated by wave or platform motions.

Errors in the fit to an assumed eddy cascade are quantified by an uncertainty $\sigma_{\epsilon\pm}$, the propagated RMSE of the fit, and by N, the noise intercept of the fit. In general, $\sigma_{\epsilon\pm} \ll \bar{\epsilon}$ (see uncertainty bars in lower panels of Figures 4 & 8) and $N \ll A(z)r^{2/3}$ (see intercepts in middle panels of Figures 4 & 8). More importantly, these values are uncorrelated with changes in wave conditions (see lower panels of Figures 5 & 9).

Errors from the pulse-coherent Doppler velocity measurements are more difficult to quantify, although they are implicit to the values of $\sigma_{\epsilon\pm}$ and N discussed above. A threshold for pulse correlation commonly is used to remove spurious points (e.g., Rusello (2009); Feddersen (2010)), and the choice of $c > 50$ (out of 100) is evaluated relative to the implicit error N. Figures 10 & 11 shows the distribution of N over all bursts and all vertical bins for four different values of correlation cutoffs. Also shown are vertical lines with the expected range $-2\sigma_u^2 < N < 2\sigma_u^2$ given a Doppler velocity uncertainty of $\sigma_u = 0.025$ m/s, or 5% of the along-beam velocity range. The noise intercept N tends to be normally distributed for a given depth z, as expected for 'white noise'. There is a trend towards narrower distributions with higher correlation cutoffs, although there are notable differences between the two field tests.

For the Duck FRF tests (Figure 10), the overall effect of the correlation threshold on noise N distributions is minimal, and noise intercepts are generally within the $\pm 2\sigma^2$ range. This is in contrast to the substantial quality control applied in the burst examples (e.g., Figure 2), however it must be noted that full quality control includes an amplitude threshold $a > 30$ which removes points in air (that also have low correlations). There is a trend towards larger N values for deeper z locations. These locations have fewer points in the fit, owing to the one-sided (i.e., downwards) differencing in the structure function calculation (Eq. 2), and are controlled by small r values. The trend in N thus may be related to the triangular bin weighting used in Nortek's processing, which results in some overlap in velocity information

between neighboring bins (i.e., at $r = 0.04$ m).

For the Lake WA tests (Figure 11), the overall effect of the correlation threshold on noise N distributions is more significant, and consistent normal distributions at all depths are only observed for $c > 50$ and $c > 75$. This suggests that the correlation cutoff $c > 50$ is important for obtaining robust $\bar{\epsilon}(z)$ estimates. The noise intercepts N are generally more negative, compared with the Duck FRF tests, and are centered at the edge of the $-2\sigma^2$ range. The more negative N values on Lake WA may be the result of peak waves ($f_p = 0.33$ Hz) that are closer to the natural frequency of the SWIFT ($f_n = 0.7$ Hz) and may cause increased motion contamination relative to the peak waves during the Duck FRF testing ($f_p = 0.1$ Hz).

Although there is no known parametric dependence or clear empirical value, it is evident from the burst examples (Figures 2 & 6) and full data sets (Figures 10 & 11) that a higher correlation cutoff improves the quality of the dissipation rate estimates, at least within the constraint of removing too many points to obtain robust statistics. Testing selected values suggests that $c > 50$ is reasonable cutoff. For the SWIFT measurements, evaluation of the pulse correlations may be more important in assessing the potential for surface reflections than in quality controlling individual points. Restated, a random distribution of low correlations will have a minimal effect on the determination of dissipation rates, but a concentration of low correlations at particular depth indicates acoustic contamination via surface reflection that may severely deteriorate the quality of dissipation estimates using a structure function method.

Finally, the noise intercepts and uncertainties provide guidance on the minimum values of dissipation that may be obtained from the SWIFT observations. Using the $\sigma = 0.025$ m/s value, the minimum dissipation rate for $N < Ar^{2/3}$ is $\bar{\epsilon}_{min} = 0.0372$ W/m^3[$= 3.7 \times 10^{-5}$ Kg/m^3]. The minimum depth integrated dissipation rate is then $\bar{E}_{min} = 0.0238$ W/m^2. These minima are admittedly large in general oceanographic terms, however they are at least an order of magnitude smaller than any of the results during field tests (or any of the

magnitudes estimated from simple analytic energy budgets). In addition, these minima are smaller than the typical uncertainties $\sigma_{\epsilon\pm} \sim 0.1$ W/m^3 and $\sigma_{E\pm} \sim 0.05$ W/m^2. Clearly, future application of SWIFT-based dissipation rates must be careful to only evaluate results well above these minima and well above the respective uncertainty values.

6. Conclusion

A new wave-following platform, termed the Surface Wave Instrument Float with Tracking (SWIFT), is used to estimate the dissipation rate of turbulent kinetic energy within the upper half-meter of the ocean. Motion data are used to estimate the wave conditions and to evaluate the degree of motion contamination. Pulse-coherent Doppler velocity data are used to determine the spatial structure of the near-surface turbulence and thereby estimate burst-averaged dissipation rates as a function of depth and time. The approach is demonstrated in two field tests under markedly different conditions (shallow-water surf breaking versus deep water whitecap breaking). In both cases, motion contamination is small and error propagation indicates robust estimates of dissipation. The advantages of the wave-following reference frame, in particular observations above the still water level and along a spatial gradient (e.g., depth or fetch), are evident in the field tests.

Acknowledgments.

Thanks to APL-UW Field Engineers J. Talbert and A. deKlerk for tireless efforts in the design, assembling, testing, deployment, and recovery of the SWIFTs. Thanks to the US-ACE Field Research Facility (FRF) staff J. Hanson and K. Hathaway for excellent logistical support, array data, and bathymetry surveys. Thanks to C. Chickadel, D. Clark, M. Haller, D. Honegger, A. Jessup, E. Williams and G. Wilson for daily shore support during FRF tests and to M. Schwendeman for help with Lake Washington tests. Thanks to F. Feddersen, ,G. Farquharson, J. Gemmrich, G. Gerbi, R. Holman, and P. J. Rusello for many

helpful discussions and comments on the manuscript. Funding provided by the National Science Foundation, the Office of Naval Research, and the University of Washington Royalty Research Fund.

REFERENCES

Agrawal, Y., E. A. Terray, M. A. Donelan, P. A. Hwang, A. J. W. III, W. M. Drennan, K. Kahma, and S. A. Krtaigorodski, 1992: Enhanced dissipation of kinetic energy beneath surface waves. *Nature*, **359**, 219–220, doi:10.1038/359219a0.

Babanin, A. V., 2011: *Breaking and dissipation of ocean surface waves*. Cambridge Univ. Press.

Banner, M. L. and D. H. Peregrine, 1993: Wave breaking in deep water. *Annu. Rev. Fluid Mech.*, **25**, 373–397.

Battjes, J., 1988: Surf-zone dynamics. *Annu. Rev. Fluid Mech.*, **20**, 257–293.

Bryan, K. R., K. P. Black, and R. M. Gorman, 2003: Spectral estimates of dissipation rate within and near the surf zone. *J. Phys. Oceanogr.*, **33**, 979–993.

Craig, P. D. and M. L. Banner, 1994: Modeling wave-enhanced turbulence in the ocean surface layer. *J. Phys. Oceanogr.*, **24**, 2546–2559.

Donelan, M., F. W. Dobson, S. D. Smith, and R. J. Anderson, 1993: On the dependence of sea surface roughness on wave development. *J. Phys. Oceanogr.*, **23**, 2143–2149.

Elgar, S., T. H. C. Herbers, and R. T. Guza, 1994: Reflection of ocean surface waves from a natural beach. *J. Phys. Oceanogr.*, **24**, 1503–1511.

Elgar, S., B. Raubenheimer, and R. T. Guza, 2001: Current meter performance in the surf zone. *J. Atmos. Ocean. Tech.*, **18**, 1735–1746.

Feddersen, F., 2010: Quality controlling surf zone acoustic doppler velocimeter observations to estimate the turbulent dissipation rate. *J. Atmos. Ocean. Tech.*, **27 (12)**, 2694–2696.

Feddersen, F., 2011: Observations of the surfzone turbulent dissipation rate. *J. Phys. Oceanogr.*

Gemmrich, J., 2010: Strong turbulence in the wave crest region. *J. Phys. Oceanogr.*, **40**, 583–595, URL DOI:10.1175/2009JPO4179.1.

Gemmrich, J., T. Mudge, and V. Polonichko, 1994: On the energy input from wind to surface waves. *J. Phys. Oceanogr.*, **24**, 2413–2417.

Gemmrich, J. R. and D. Farmer, 1999: Observations of the scale and occurrence of breaking surface waves. *J. Phys. Oceanogr.*, **29**, 2595–2606.

Gemmrich, J. R. and D. Farmer, 2004: Near-surface turbulence in the presence of breaking waves. *J. Phys. Ocean.*, **34**, 1067–1086.

Gerbi, G., J. Trowbridge, E. Terray, A. J. Plueddemann, and T. Kukulka, 2009: Observations of turbulence in the ocean surface boundary layer: energetics and transport. *J. Phys. Oceanogr.*, **39**, 1077–1096.

Graber, H., E. Terray, M. Donelan, W. Drennan, J. V. Leer, and D. Peters, 2000: Asis- a new air-sea interaction spar buoy: design and performance at sea. *J. Atmos. Ocean. Tech.*, **17 (5)**, 708–720.

Herbers, T. H. C., N. R. Russnogle, and S. Elgar, 2000: Spectral energy balance of breaking waves within the surf zone. *J. Phys. Oceanogr.*, **30**, 2723–2737.

Kolmogorov, A. N., 1941: Dissipation of energy in the locally isotropic turbulence. *Dokl. Akad. Nauk SSR*, **30**, 301–305.

Lumley, J. L. and E. A. Terray, 1983: Kinematics of turbulence convected by a random wave field. *J. Phys. Oceanogr.*, **13**, 2000–2007.

MacMahan, J., J. Brown, and E. Thornton, 2009: Low-cost handheld gps for measuring surf-zone currents. *J. Coastal Res.*, **25 (3)**, 744–754.

588 Mei, C., 1989: *The Applied Dynamics of Ocean Surface Waves*, Advanced Series on Ocean
589 Engineering, Vol. 1. World Scientific.

590 Melville, W. K., 1996: The role of surface-wave breaking in air-sea interaction. *Annu. Rev.*
591 *Fluid Mech.*, **28**, 279–321.

592 Middleton, F., L. LeBlanc, and M. Czarnecki, 1976: Spectral tuning and calibration of a
593 wave following buoy. *Offshore Technology Conference, 3-6 May , Houston, Texas.*

594 Pascal, R. W., et al., 2011: A spar buoy for high-frequency wave measurements and detection
595 of wave breaking in the open ocean. *J. Atmos. Ocean. Tech.*, **28**, 590–605.

596 Rusello, P. J., 2009: A practical primer for pulse coherent instruments. Tech. Rep. TN-027,
597 Nortek AS.

598 Rusello, P. J. and E. Cowen, 2011: Turbulent dissipation estimates from pulse coherent
599 doppler instruments. *Current, Waves and Turbulence Measurements (CWTM).*

600 Schmidt, W. E., B. T. Woodward, K. S. Milikan, R. T. Guza, B. Raubenheimer, and S. Elgar,
601 2003: A gps-tracked surf zone drifter. *J. Atmos. Ocean. Tech.*, **20**, 1069–1075.

602 Spydell, M., F. Feddersen, R. T. Guza, and W. E. Schmidt, 2007: Observing surf-zone
603 dispersion with drifters. *Journal of Physical Oceanography*, **37 (12)**, 2920–2939, doi:10.
604 1175/2007JPO3580.1, URL `http://dx.doi.org/10.1175/2007JPO3580.1`.

605 Terray, E., M. Donelan, Y. Agrawal, W. Drennan, K. Kahma, A. Williams, P. Hwang, and
606 S. Kitaigorodskii, 1996: Estimates of kinetic energy dissipation under breaking waves. *J.*
607 *Phys. Oceanogr.*, **26**, 792–807.

608 Thomson, J., A. Jessup, and J. Gemmrich, 2009: Energy dissipation and the spectral distri-
609 bution of whitecaps. *Geophys. Res. Let.*, **36**.

610 Trowbridge, J. and S. Elgar, 2001: Turbulence measurements in the surf zone. *J. Phys.*
611 *Oceanogr.*, **31**, 2403–2417.

612 Wiles, P., T. P. Rippeth, J. Simpson, and P. Hendricks, 2006: A novel technique for measur-
613 ing the rate of turbulent dissipation in the marine environment. *Geophys. Res. Let.*, **33**,
614 L21 608.

615 Zedel, L., A. Hay, R. Cabrera, and A. Lohrmann, 1996: Performance of a single-beam
616 pulse-to-pulse coherent doppler profiler. *J. Ocean. Eng.*, **21 (3)**, 290–297.

List of Figures

668 7 Example SWIFT burst spectra collected in deep water on Lake Washington.
669 The left panels show moderate-breaking conditions at a short fetch distance,
670 and the right panels show strong breaking conditions at a larger fetch dis-
671 tance. Conditions are determined by GPS location, and by the onboard video
672 images shown in the upper panels. Middle panels show wave height spectra
673 (from SWIFT GPS data) and SWIFT platform motion spectra (pitch, roll,
674 heading, and pressure from the SWIFT Aquadopp HR). Lower panels show
675 velocity spectra, including wave orbital motion (from SWIFT GPS data) and
676 turbulence at one selected depth (from the SWIFT Aquadopp HR data). Also
677 shown are spectra of differences between select depths of the turbulence pro-
678 file, which is the relevant quantity for calculating the structure function. 39
679 8 Example SWIFT burst results collected in deep water on Lake Washington.
680 The left panels show moderate-breaking conditions at a short fetch distance,
681 and the right panels show strong breaking conditions at a larger fetch distance.
682 Conditions are determined by GPS location, and by the onboard video images
683 shown in the upper panels. The middle panels show the structure function
684 $D(z, r)$ (Eq. 2) and associated fits $Ar^{2/3} + N$ (Eq. 3) as dots and lines,
685 respectively. Colors indicate depth beneath the wave following surface. The
686 lower panels show the resulting depth profiles of dissipation rate $\bar{\epsilon}(z)$, with
687 horizontal bars for uncertainties $\sigma_{\epsilon\pm}$. The corresponding ADV estimates at
688 $z = 0.25$ m are shown in green. 40

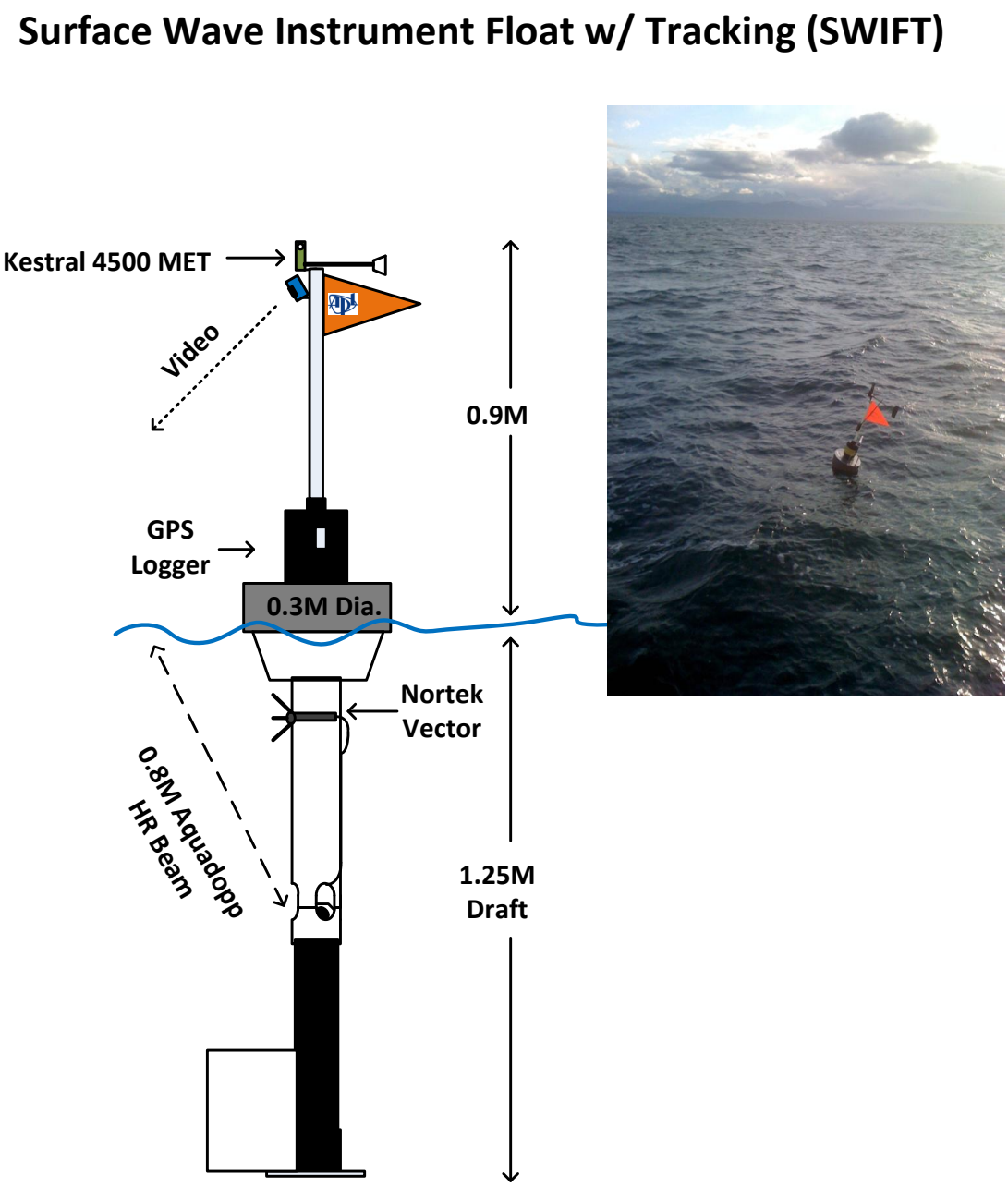

FIG. 1. (a) Dimensional drawing and (b) picture of a SWIFT: Surface Wave Instrument Float with Tracking. Drawing courtesy of J. Talbert, APL-UW.

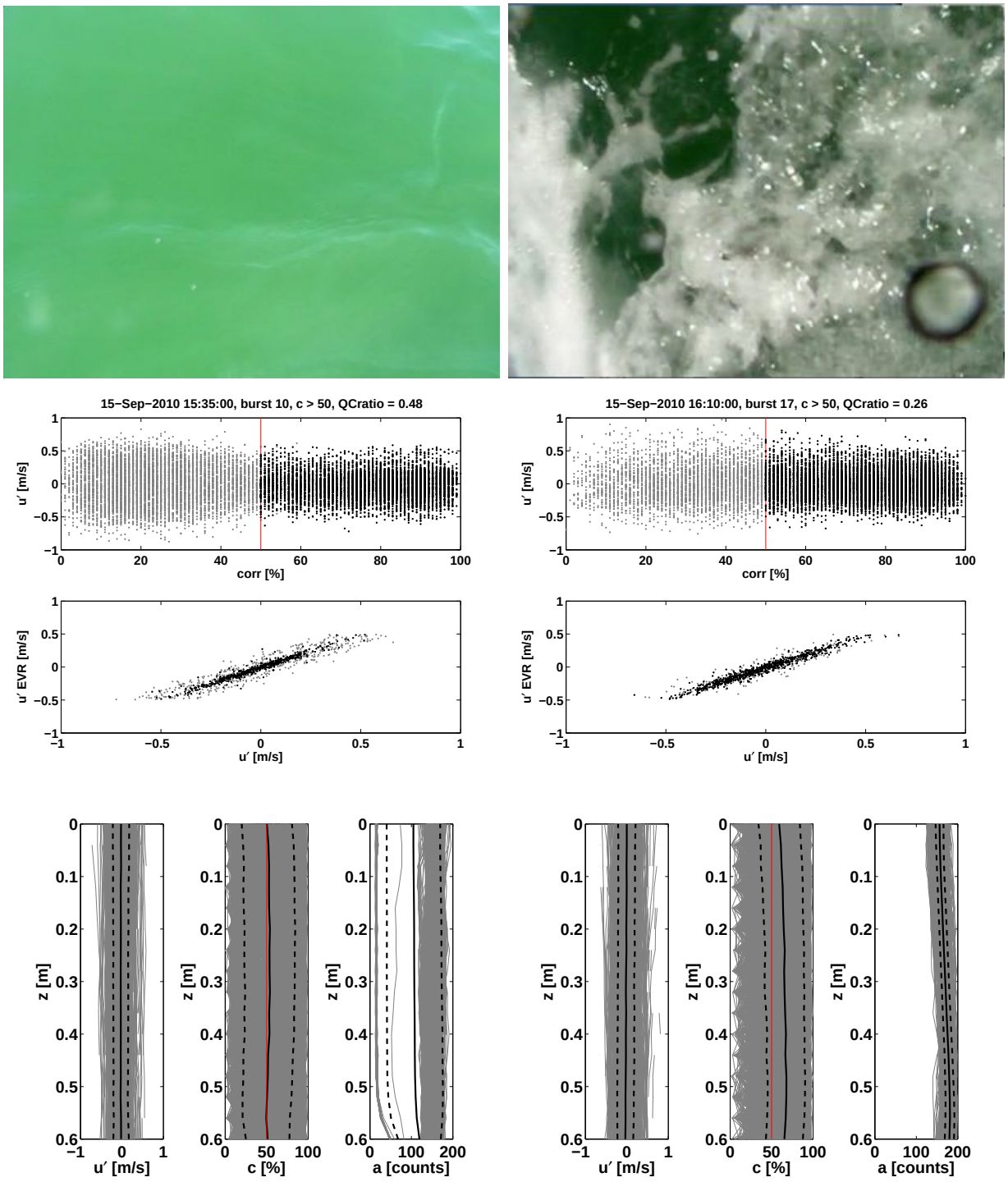

FIG. 2. Example raw SWIFT burst data collected in shallow water at the Duck FRF. The left panels show non-breaking conditions outside of the surf zone, and the right panels show breaking conditions within the surf zone. Conditions are determined by GPS location, and by the onboard video images shown in the upper panels. Velocity data quality control, using pulse-pulse correlation and extended velocity range, is shown in the middle panels. The lower panels show the resulting profiles of turbulent velocity $u'(z)$, correlation $c(z)$, and backscatter amplitude $a(z)$. Thick lines are mean values and dashed lines are $\pm$ one standard deviation.

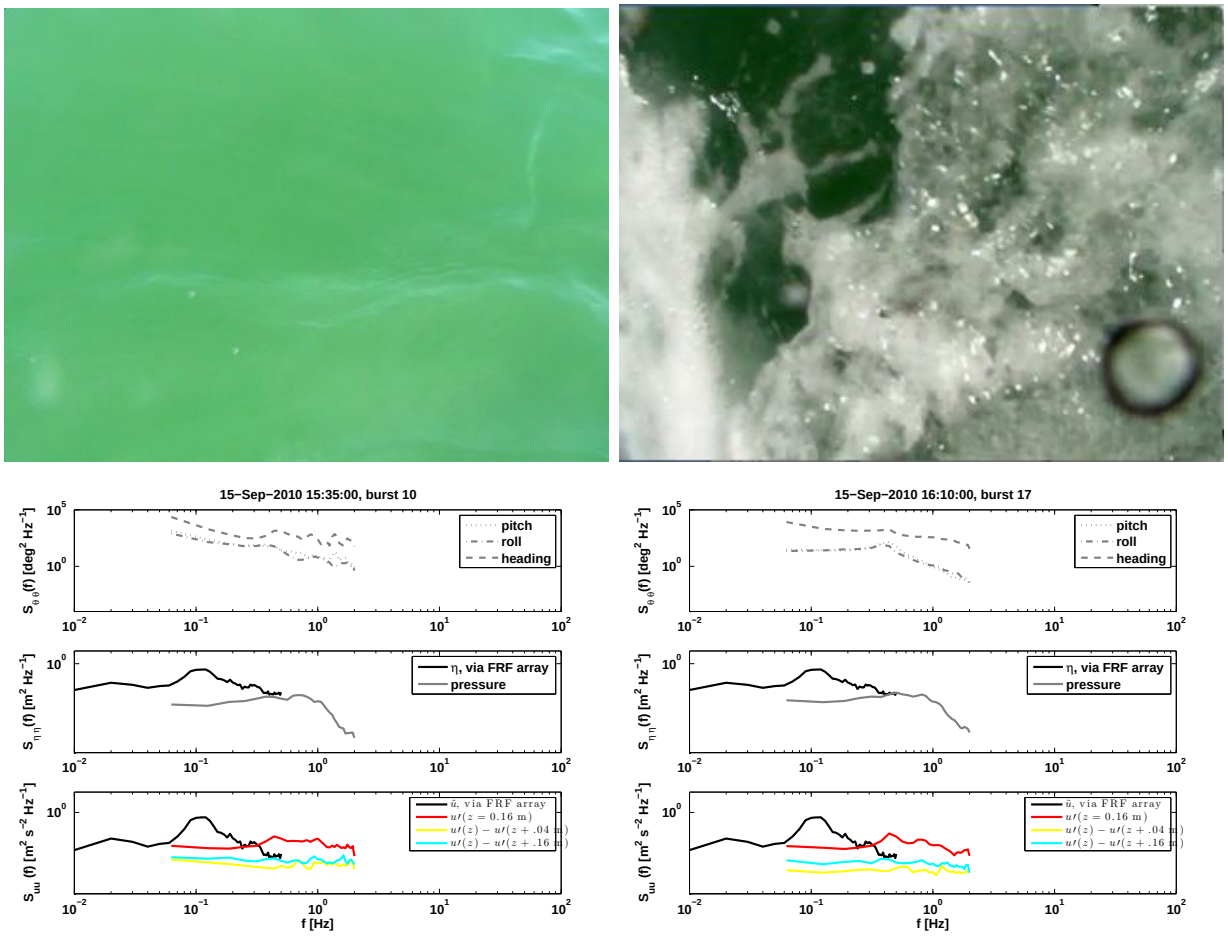

FIG. 3. Example SWIFT spectra collected in shallow water at the Duck FRF. The left panels show non-breaking conditions outside of the surf zone, and the right panels show breaking conditions within the surf zone. Conditions are determined by GPS location, and by the onboard video images shown in the upper panels. Middle panels show wave height spectra (from independent FRF measurements) and SWIFT platform motion spectra (pitch, roll, heading, and pressure from the SWIFT Aquadopp HR data). Lower panels show velocity spectra, including wave orbital motion (from independent FRF measurements) and turbulence at one selected depth (from the SWIFT Aquadopp HR data). Also shown are spectra of differences between select depths of the turbulence profile, which is the relevant quantity for calculating the structure function.

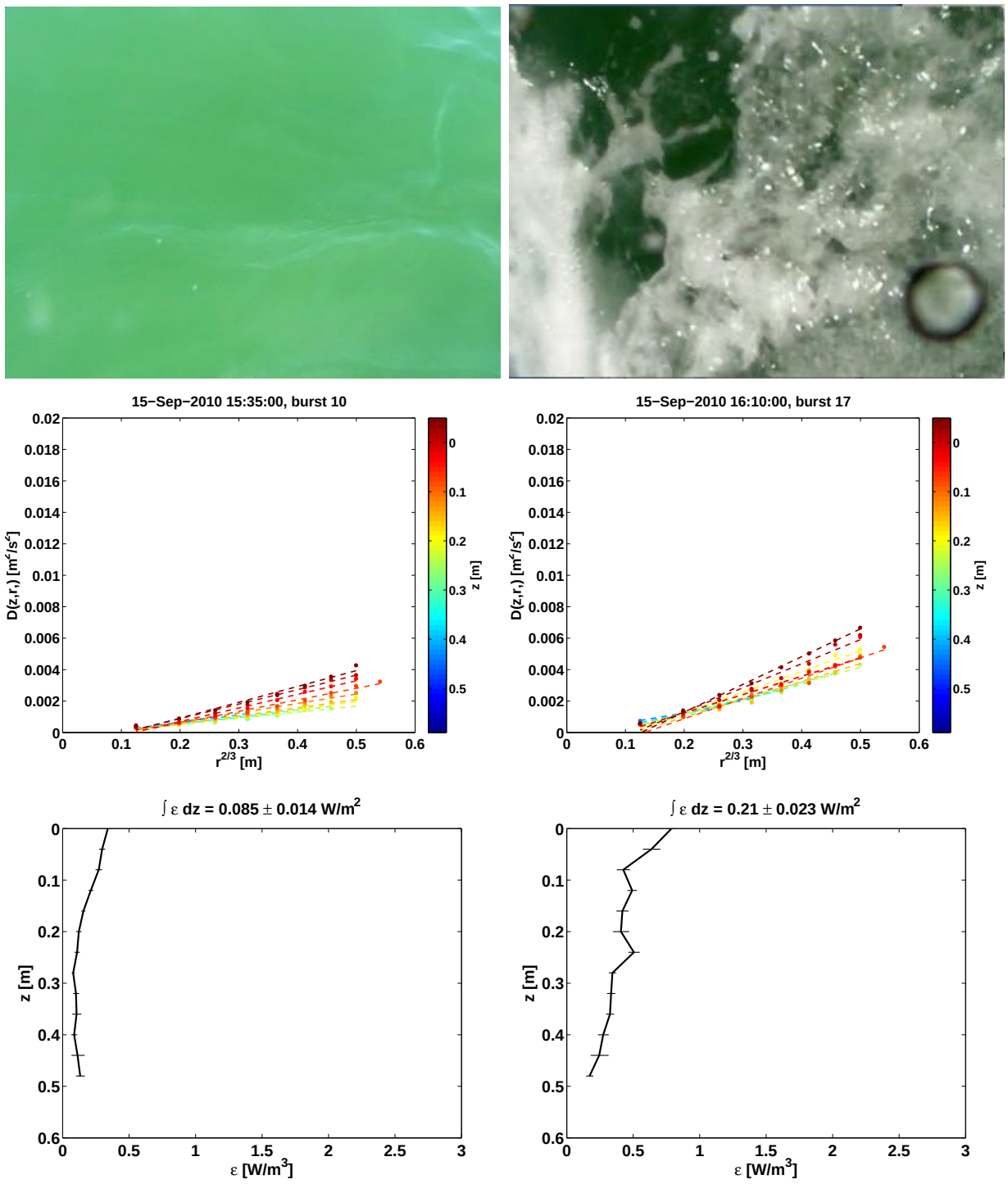

FIG. 4. Example SWIFT burst results collected in shallow water at the Duck FRF. The left panels show non-breaking conditions outside of the surf zone, and the right panels show breaking conditions within the surf zone. Conditions are determined by GPS location, and by the onboard video images shown in the upper panels. The middle panels show the structure function $D(z,r)$ (Eq. 2) and associated fits $Ar^{2/3} + N$ (Eq. 3) as dots and lines, respectively. Colors indicate depth beneath the wave following surface. The lower panels show the resulting depth profiles of dissipation rate $\bar{\epsilon}(z)$, with horizontal bars for uncertainties $\sigma_{\epsilon\pm}$.

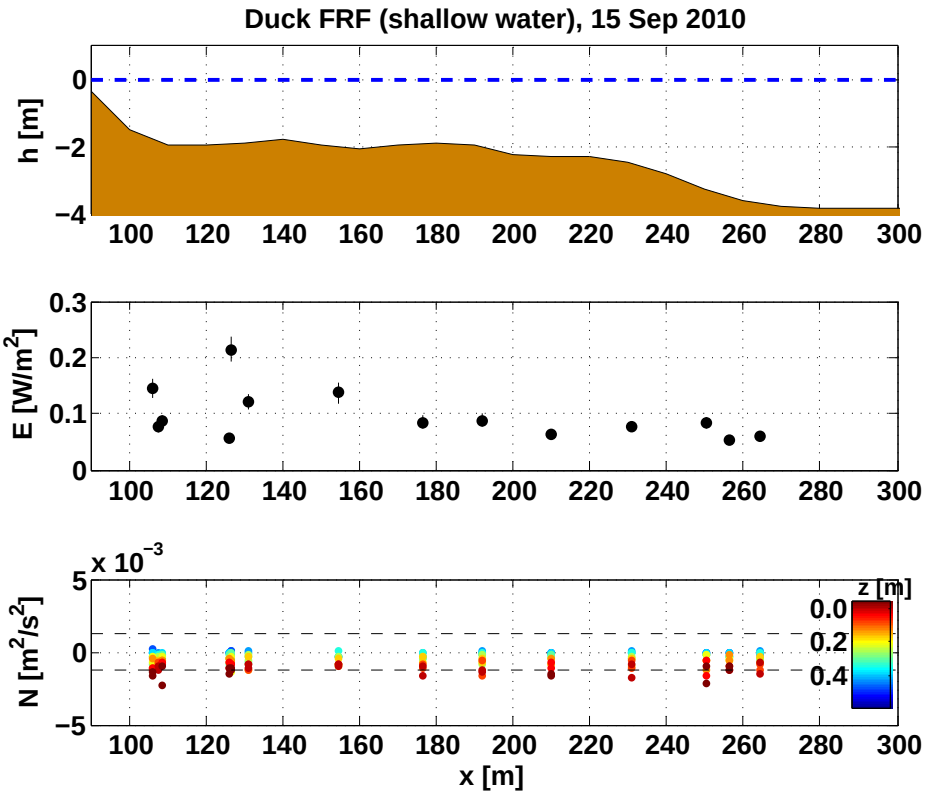

FIG. 5. Aggregated results of SWIFT drifts at the Duck FRF versus cross-shore position. Upper panel shows the nearshore bathymetry as a shaded region and the still water level as a dashed line. Middle panel shows the depth-integrated dissipation $\bar{E}$, which increases shoreward (decreasing x). Vertical bars show uncertainties $\sigma_{E\pm}$. Lower panel shows the noise intercepts N of the structure function fit, which are approximately uniform at all cross-shore positions. Colors indicate depth beneath the wave following surface, as in Figure 4. The FRF instrument (bottom-mounted Aquadopp) used for wave spectra in Figure 3 is located at $x = 232$ m.

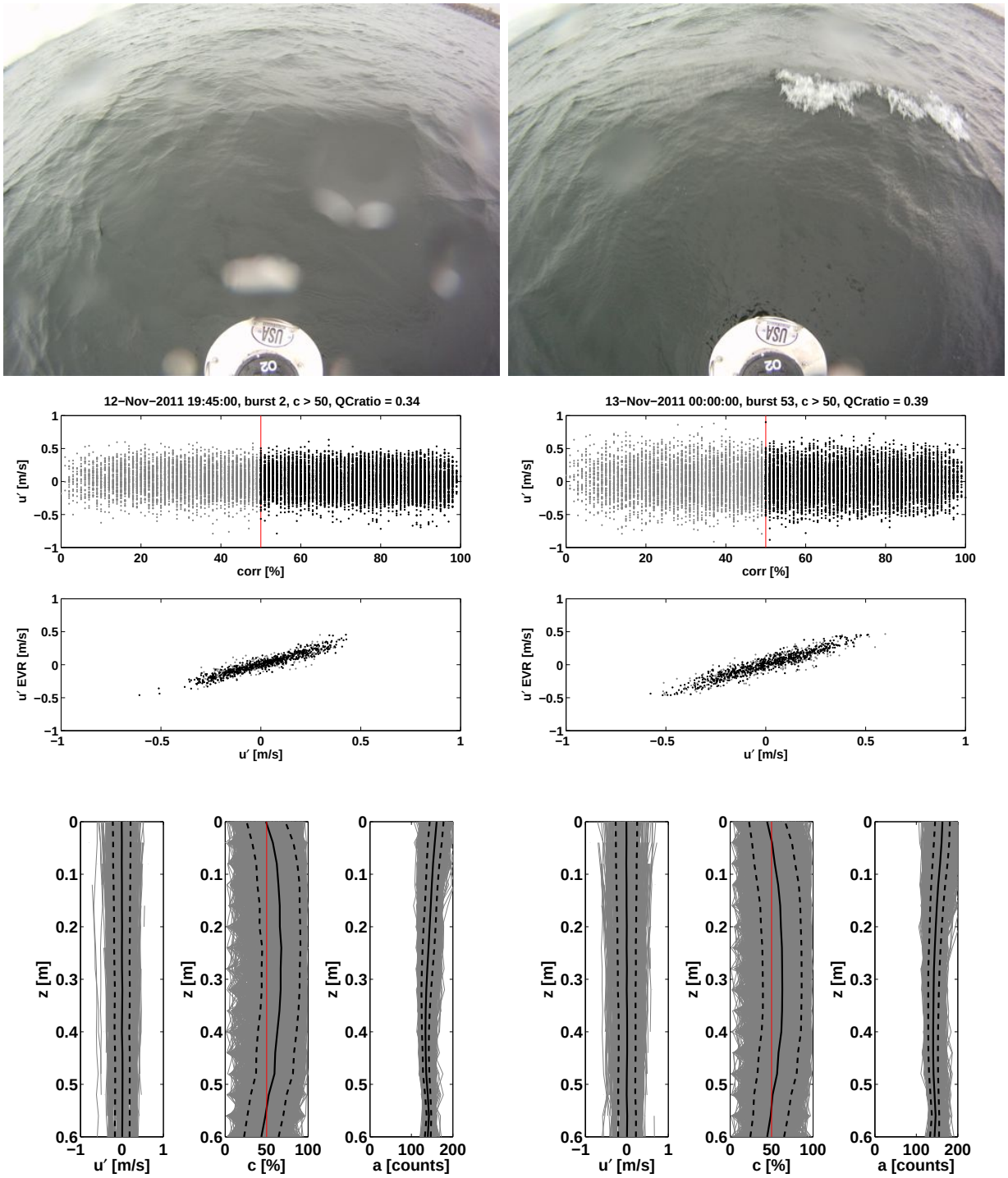

FIG. 6. Example raw SWIFT burst data collected in deep water on Lake Washington. The left panels show moderate-breaking conditions at a short fetch distance, and the right panels show strong breaking conditions at a larger fetch distance. Conditions are determined by GPS location, and by the onboard video images shown in the upper panels. Velocity data quality control, using pulse-pulse correlation and extended velocity range, is shown in the middle panels. The lower panels show the resulting profiles of turbulent velocity $u'(z)$, correlation $c(z)$, and backscatter amplitude $a(z)$. Thick lines are mean values and dashed lines are $\pm$ one standard deviation.

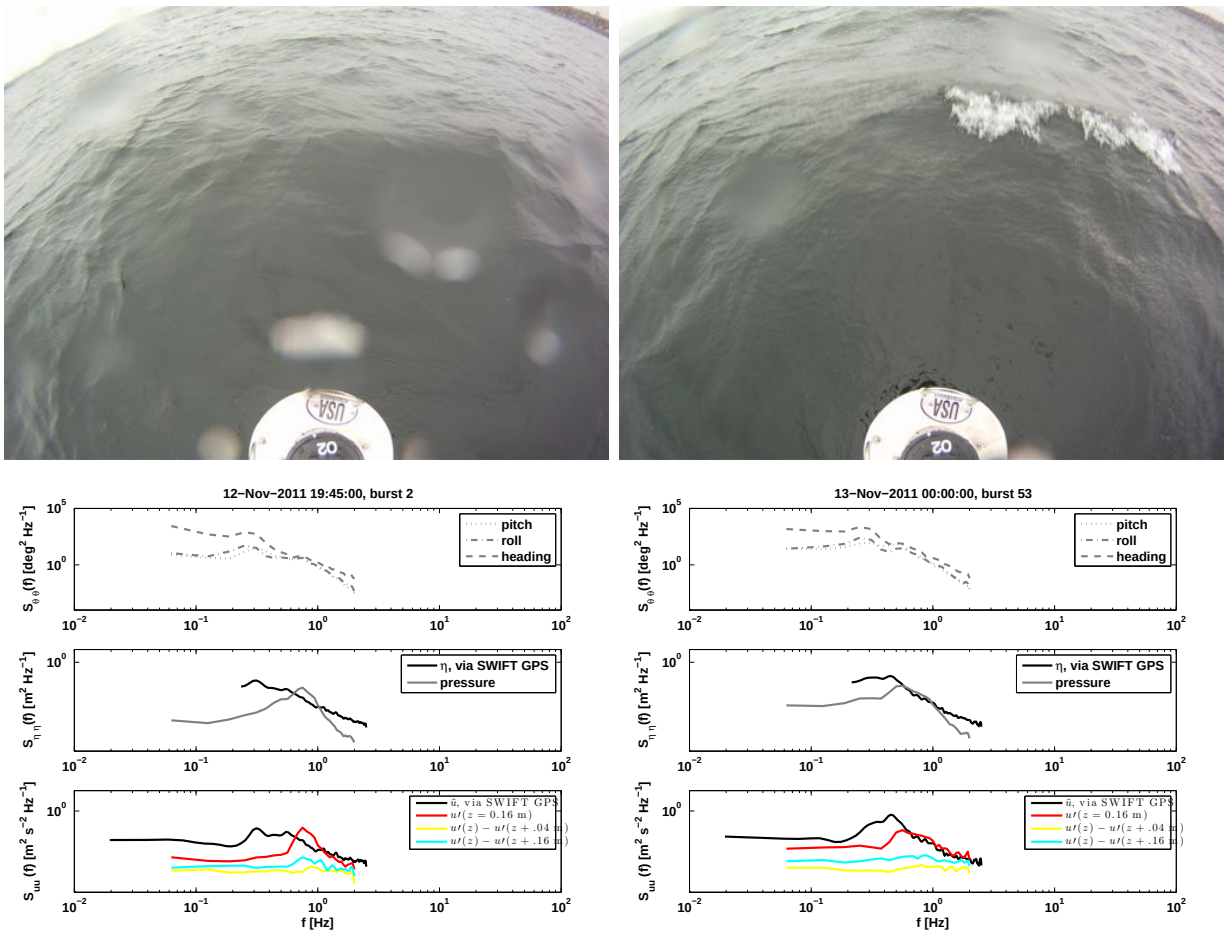

FIG. 7. Example SWIFT burst spectra collected in deep water on Lake Washington. The left panels show moderate-breaking conditions at a short fetch distance, and the right panels show strong breaking conditions at a larger fetch distance. Conditions are determined by GPS location, and by the onboard video images shown in the upper panels. Middle panels show wave height spectra (from SWIFT GPS data) and SWIFT platform motion spectra (pitch, roll, heading, and pressure from the SWIFT Aquadopp HR). Lower panels show velocity spectra, including wave orbital motion (from SWIFT GPS data) and turbulence at one selected depth (from the SWIFT Aquadopp HR data). Also shown are spectra of differences between select depths of the turbulence profile, which is the relevant quantity for calculating the structure function.

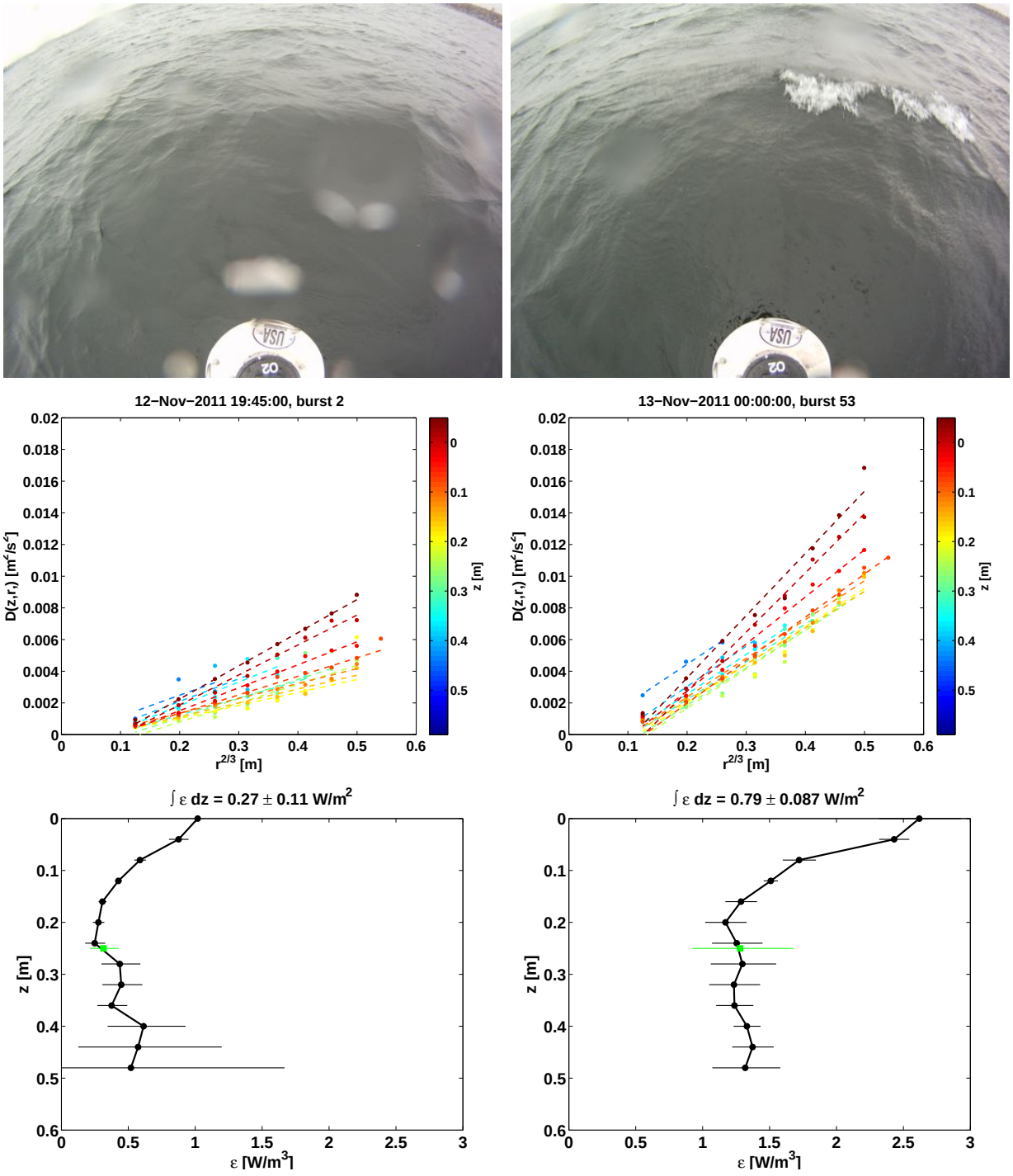

FIG. 8. Example SWIFT burst results collected in deep water on Lake Washington. The left panels show moderate-breaking conditions at a short fetch distance, and the right panels show strong breaking conditions at a larger fetch distance. Conditions are determined by GPS location, and by the onboard video images shown in the upper panels. The middle panels show the structure function $D(z,r)$ (Eq. 2) and associated fits $Ar^{2/3}+N$ (Eq. 3) as dots and lines, respectively. Colors indicate depth beneath the wave following surface. The lower panels show the resulting depth profiles of dissipation rate $\bar{\epsilon}(z)$, with horizontal bars for uncertainties $\sigma_{\epsilon\pm}$. The corresponding ADV estimates at $z = 0.25$ m are shown in green.

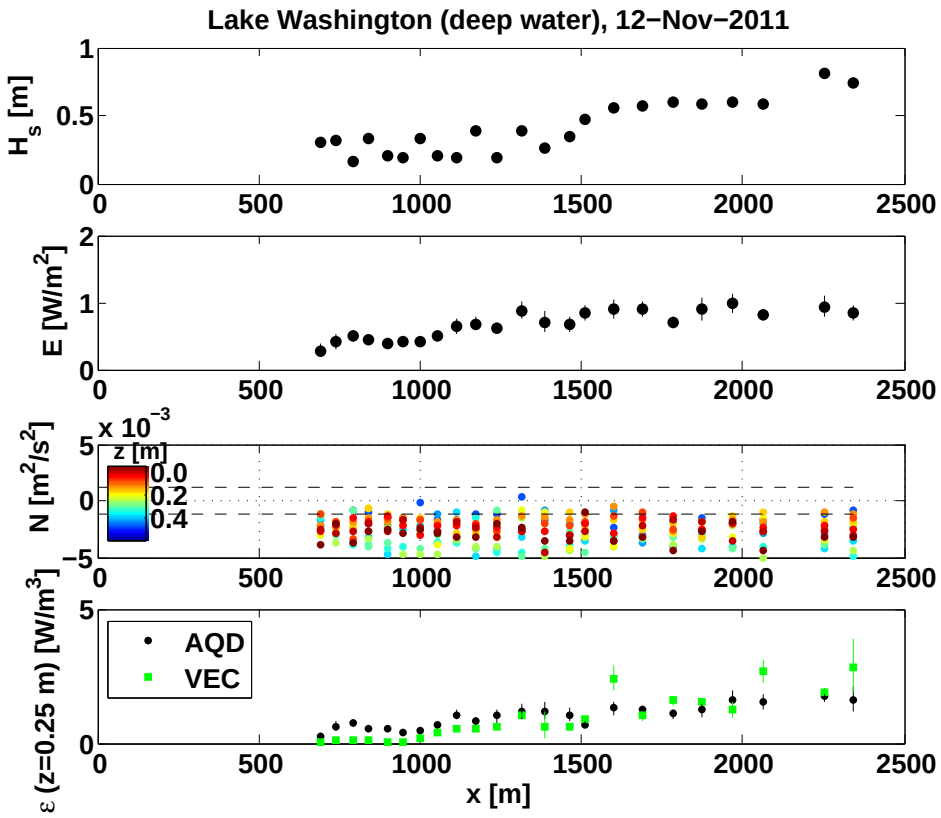

FIG. 9. Aggregated results of SWIFT drifts on Lake WA versus fetch x. Upper panel shows the significant wave height estimated from the SWIFT GPS spectra as $H_s = 4\sqrt{\int S_{\eta\eta}(f)df}$. Upper-middle panel shows the depth-integrated dissipation $\bar{E}$. Vertical bars show uncertainties $\sigma_{E\pm}$. Lower-middle panel shows the noise intercepts N of the structure function fit, which are approximately uniform at all fetch. Colors indicate depth beneath the wave following surface, as in Figure 8. Lower panel shows the comparison of dissipation rate $\bar{\epsilon}(z = 0.25$ m) obtained from the Aquadopp (AQD) structure function and the acoustic Doppler velocimeter (ADV) spectra.

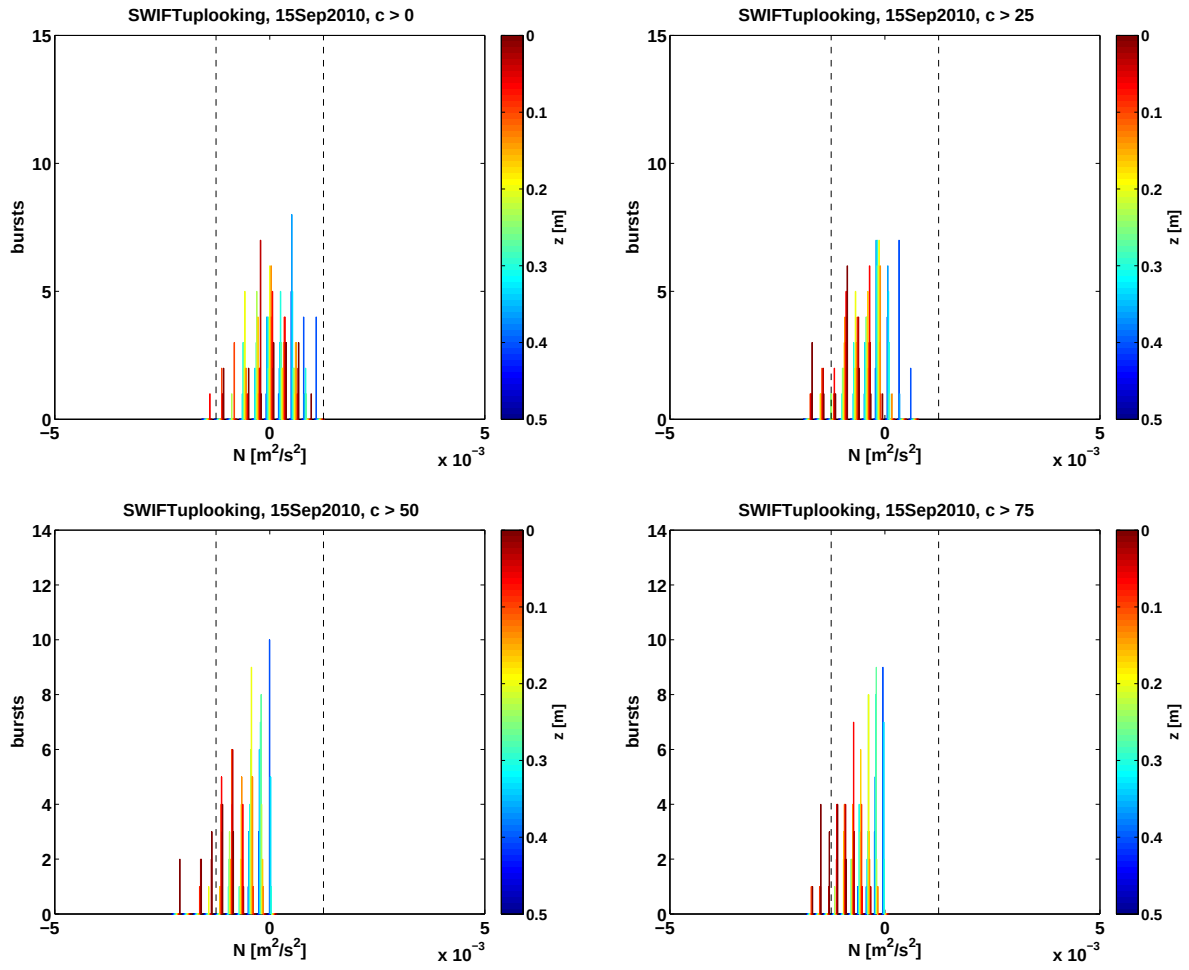

FIG. 10. Distributions of noise intercepts N from all bursts at Duck FRF using four different pulse correlation cutoffs for quality control of velocity data. Clockwise from upper-left: $c > 0, c > 25, c > 75, c > 50$. Colors indicate depth beneath the wave following surface, as in Figure 4. Dashed lines indicate the excepted range for N, given a Doppler velocity uncertainty of $\sigma_u = 0.025$ m/s.

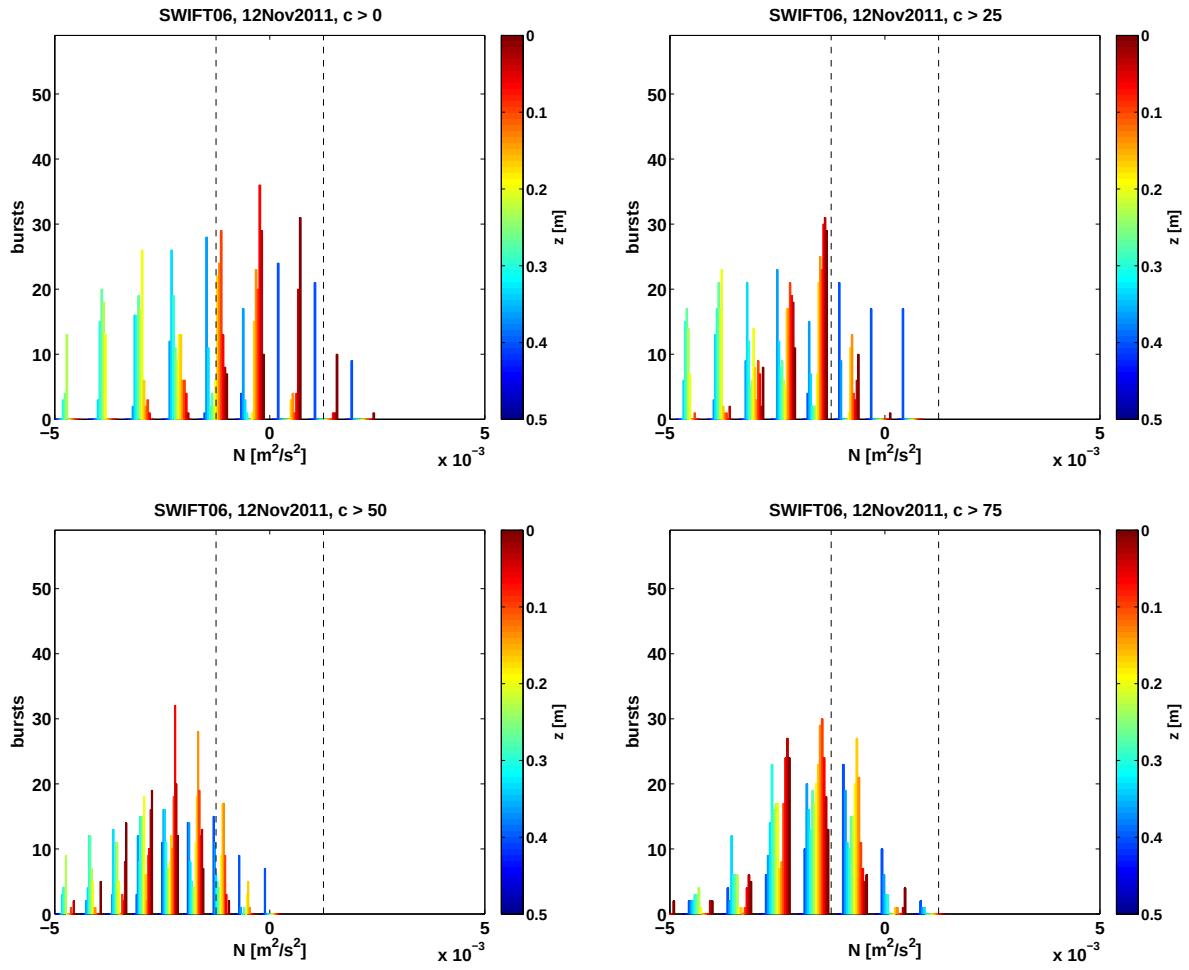

FIG. 11. Distributions of noise intercepts N from all bursts on Lake WA using four different pulse correlation cutoffs for quality control of velocity data. Clockwise from upper-left: $c > 0, c > 25, c > 75, c > 50$. Colors indicate depth beneath the wave following surface, as in Figure 8. Dashed lines indicate the excepted range for N, given a Doppler velocity uncertainty of $\sigma_u = 0.025$ m/s.